The reachable 3-D workspace volume is a measure of payload and body-mass-index

A quasi-static kinetic assessment

Castro, Miguel Nobre; Rasmussen, John; Bai, Shaoping; Andersen, Michael Skipper

Published in:
Applied Ergonomics

DOI (link to publication from Publisher):
10.1016/j.apergo.2018.09.010

Publication date:
2019

Document Version
Accepted author manuscript, peer reviewed version

The reachable 3-D workspace volume is a measure of payload and body-mass-index: a quasi-static kinetic assessment

Miguel Nobre Castro[a,1](✉), John Rasmussen[a,2], Shaoping Bai[a,3], Michael Skipper Andersen[a,4]
Department of Materials and Production, Fibigerstraede 16, Aalborg University, DK-9220 Aalborg East, Denmark
[1]mnc@mp.aau.dk, [2]jr@mp.aau.dk, [3]shb@mp.aau.dk, [4]msa@mp.aau.dk

Corresponding Author: (✉) Miguel Nobre Castro

ABSTRACT

An experimental protocol with five tasks is proposed for a low-cost empirical assessment of the reachable 3-D workspace (RWS), including both close-to-torso and far-from-torso regions.

Ten participants repeated the protocol for four distinct hand payloads. The RWS expressed as a point cloud and its non-convex alpha-shape were obtained for each case. Moreover, individual strength surrogates for glenohumeral flexion and abduction, and elbow flexion were collected using a dynamometer. The RWS volume was statistically modelled using payload, body-mass-index and the strength surrogates as predictors.

For increasing payload, a significant ($r=-0.736, p<0.001$) decrease in RWS volume was found for distinct payload cases across all subjects. The only significant predictors found for the RWS volume were normalized payload ($F=73.740, p<0.001$) and body-mass-index ($F=11.008, p=0.003$). No significant interactions were found. The consequent regression model ($F(2,27)=41.11$, $p<0.001$, $R^2_{adj}=0.7345$) explained around 73% of the variation in the data.

The RWS volume is a function of payload and body-mass-index.

Keywords: Reachable Workspace; Strength Measurements; Upper Extremity Kinematics; Statistical Modelling

1. INTRODUCTION

The reachable 3-D workspace (RWS) is used in the field of robotics when analysing manipulators and kinematic chains. Siciliano et al. (2009) described the RWS as the region that the origin of the end-effector's frame of a manipulator can reach with at least one orientation, and its volume is typically used as a performance metric. Conversely, the RWS can be applied in the fields of biomechanics, ergonomics, and even directly used as a clinical outcome/metric. Anatomically speaking, the human RWS can be estimated from a reference point in the hand or wrist (Lenarcic and Umek, 1994). The study of this RWS provides an insight into upper extremity function for both healthy and impaired individuals. It is likewise suitable for designing ergonomic equipment such as devices for specific working environments (Sengupta et al., 2000; Sengupta and Das, 2004) or exoskeletons capable of augmenting strength and endurance (Schiele and van der Helm, 2006). For the RWS, close-to-torso and far-from-torso reaching regions can be defined. Some authors only report the far-from-torso region as the maximum RWS (Johnston et al., 2015; Kurillo et al., 2012; Sengupta and Das, 1998) or simply subtract the torso volume from an extrapolated RWS envelope (Klopčar and Lenarčič, 2005).

However, vital activities of daily living (ADL), such as feeding or even precision tasks in a workstation, fall mainly in the close-to-torso region. Thus, RWS movement protocols capable of capturing performance in the close-to-torso region are important and missing in the literature. The RWS can be generated either empirically, by fitting a spherical surface to experimental data (Kurillo et al., 2012; Sengupta and Das, 1998), or from kinematic models representing the upper extremity as a manipulator (Klopčar et al., 2007; Matthew et al., 2015; Yang et al., 2005). In each case, respectively, the experimental input data are directly the position coordinates of a distal point in the hand or wrist in relation to a fixed reference frame or the measured subject's active range-of-motion (ROM).

Regarding the use of kinematic models, the RWS's envelope corresponds to configurations in which one or more joints are at their limits or to kinematically singular postures resulting from aligned links or joint axes (Yang et al. 2005). Nevertheless, kinematic models are helpful to generate RWS from the anatomical joints' ROM, given that the shoulder complex does not behave as a pure spherical joint, due to coupled motions generated from the sternoclavicular, acromioclavicular and scapulothoracic joints (Klopčar et al., 2007; Klopčar and Lenarčič, 2005). To minimize the computational cost of these models, Matthew et al. (2015) suggested Monte-Carlo sampling of the joint space, rather than sweeping all combinations of degrees-of-freedom (DOF).

In contrast, empirical methods based on fitting a sphere to the experimental data are very attractive due to their fast assessment and simplistic protocol, but they have an important shortcoming in neglecting the close-to-torso region. As an example, an impaired subject, who cannot perform elbow flexion, is unable to feed himself despite being able to reach the far-from-torso region.

Park (2007) found the dependency of the RWS on anatomical joint moment strength, body weight and hand payload using a planar kinematic model, while addressing isometric strength. Johnston et al. (2015) showed experimentally that the maximum reachable distance (far-from-torso) decreases as the hand payload increases. Such findings are relevant as both ADL and workstation labour often require reaching, grasping and moving objects with distinct masses at distinct heights within the RWS. The experimental set-ups require, however, a computerized potentiometric measurement system (Sengupta et al., 2000; Sengupta and Das, 1998), which not only brings an additional cost but also has its own physical limitation while measuring the RWS (Johnston et al., 2015). Thus, this article proposes a versatile, three-dimensional, kinetic RWS measurement protocol including the close-to-torso region. This provide volumetric information capable of characterizing different subjects.

Therefore, this study aimed at defining a measurement protocol to assess the RWS including both far-from-torso and close-to-torso regions. The alpha-shape algorithm (Edelsbrunner and Mücke, 1994) approximates the full 3-D volume, while capturing the close-to-torso reachable region. The variation of the RWS volume as a function of hand payload conditions was subsequently investigated. Afterwards, a multivariate regression model was used to analyse how the RWS volume varies as a function of payload and of a subject's anthropometry by separate measurements of surrogates of individual strength. Finally, we investigate and discuss the effect of possible interactions between these variables.

2. MATERIAL AND METHODS

2.1. Experimental procedures

The RWS and surrogates of individual strength were studied for a group of ten healthy adults (ten males, age 30.0±8.0 years; body mass 78.9±10.8 kg; height 1.80±0.06 m; upper extremity length 0.644±0.027 m). Non-parametric Shapiro-Wilk test of normality were performed for these variables: $p=0.4342$ for the body mass, $p=0.1574$ for the height and $p=0.4870$ for the upper extremity length (histograms and population distributions available in the Supplementary Material). Inclusion criteria were: healthy with no abnormalities in the upper extremity bone structure or missing limbs, as well as the absence of any type of injury at the time of data collection. Written informed consent was given by the participants. The ethical guidelines of The North Denmark Region Committee on Health Research Ethics were followed. The experiment comprised 1) a kinematic assessment of the RWS for four different hand payload cases and 2) an assessment of the maximum force generation capability in the direction of three specific anatomical joint movements: glenohumeral flexion and abduction, and elbow flexion – these were selected as the most relevant for counteracting gravity during a reaching situation.

For every day test, participants performed a 5-minutes warm-up consisting of random motions covering the canonical movements that span each anatomical joint in the upper extremity. A wrist stabilizing brace (Mueller® Wrist Brace, Mueller Sports Medicine Inc, Wisconsin, USA) was provided to exclude wrist joint movements from the assessment. 19 reflective markers were placed on the skin through palpation of specific bony landmarks (see Supplementary Material). An eight Opus camera setup along with Qualisys Track Manager v.2.9 (Qualisys AB, Gothenburg, Sweden) was used to collect the respective marker trajectories.

2.1.1. Kinematic assessment of the reachable 3-D workspace

Each participant was standing still for five seconds with the arms in a neutral and relaxed posture close to the anatomical reference position. An assistant then instructed each of the tasks to be performed. This aid included the mirrored performance of the movements to enhance capturing the boundaries of the RWS for every subject. The motions were always performed by starting from a medial orientation (sagittal/flexion-extension plane), progressing to the lateral orientation (frontal/abduction-adduction plane), and then moving back to the medial orientation. Simultaneously, by starting from a neutral position, the arm progressed upwards to the overhead region and moved back, downwards, to the neutral position. Demonstration videos are provided as Supplementary Material.

Five different tasks (Figure 1) inspired on the work of Rosen et al. (2005) on designing an upper limb powered exoskeleton, were defined such that the test-subjects reached both close-to-torso and far-from-torso boundaries of the RWS envelope. Bearing in mind the extension of such type of protocol to evaluate the performance of strength and endurance augmenting devices, movements were performed at a slow "quasi-static" pace. This way, highly dynamic velocities in which the arm and payload are not manipulated with control and dexterity were

avoided. These covered motions from simple ADL such as eating to harder task such as moving heavy objects. Therefore, each of the following tasks lasted about 90 seconds in order to span as much volume as possible while the trunk posture was kept vertical:

- Vertical task: 'zig-zag' motion spanning 30º angles with the elbow fully extended as if the subject is touching the surface of an imaginary sphere, reaching as far as possible;
- Horizontal task: 'zig-zag' motion spanning 30º angles with the elbow fully extended as if the subject is touching the surface of an imaginary sphere, reaching as far as possible;
- Shower task: arm motion such that the hand is randomly touching the tights, trunk and head simulating washing the body and head during a shower;
- Curls task: successive elbow flexion movements about different vertical planes rotated by 30ºdefined by different and synchronized shoulder flexion and abduction angles;
- Free-motion task: free upper extremity motion covering the inner volume delimited by the previous four tasks (this may vary from subject to subject).

[Figure 1]

Figure 1. Illustration of the five different tasks to estimate the reachable 3D-space envelope: (A) Vertical, (B) Horizontal, (C) Shower, (D) Curls, (E) Free-motion.

The five tasks were repeated for four different hand payload cases, performed in four distinct days to avoid fatigue, by using different dumbbells with different mass. Overall, these corresponded to 20 trials per subject, five per day. The first consisted of the no-payload case corresponding to the active RWS – drawing a parallel with the active ROM of a given subject. Subsequently, the other three payload cases were executed, such that they would result in a gradual decrease in the RWS volume. The idea behind this protocol was to enable a systematic analysis of the volume reduction as a function of payload and of subject-specific strength. Johnston et al. (2015) previously reported that there is no significant change of the RWS volume from light payloads such as 0.5 and 1 kg. Accordingly, after performing some prior pilot tests on other volunteers not included in this study, a shoulder abduction task with a given payload between 8 and 12 kg was used to select the dumbbell weight combinations for each test-subject. The threshold payload was defined as the middle payload case when the participant could only perform a one-repetition maximum abduction angle close to 90º at a slow pace. In order to avoid fatigue propagation, this measurement was performed on the same day as the no-payload case and the number of attempts was limited to three. The remaining two load cases were selected according to a weight increase and decrease from that threshold in steps of at least 2 kg.

2.1.2. Dynamometric assessment of the maximum force generation capability

The maximum force generation capability F_{max}, a surrogate measure for individual strength, was measured on seated subjects pulling against a dynamometer mounted on a cable fixed to the floor (Figure 2) with nearly vertical force directions in the following setups:

1. Force transducer strapped to the middle of the upper arm, 0º glenohumeral flexion, 0º elbow flexion, glenohumeral abduction varying in three attempts around 90º.
2. Force transducer strapped to the middle of the upper arm, 0º elbow flexion, 0º glenohumeral abduction, glenohumeral flexion varying in three attempts around 90º.
3. Force transducer strapped to the middle of the forearm, 0º glenohumeral flexion, 0º glenohumeral abduction, elbow flexion varying in three attempts around 90º.

The force sensor, a Universal Digital Dynamometer (Tiedemann & Betz GmbH & Co, Garmisch-Partenkirchen, Germany) with 0.1 N resolution, was connected to a computer via a

USB cable. Three extra markers (Figure 2) were added to the dynamometer and to the dynamometer arm attachment band, either on the middle of the upper arm or forearm.

Instructions were given to each participant to lean against the backrest without moving the trunk to avoid postural compensation. The participants were vocally encouraged to maximize voluntary contraction. In the post-processing of the results, the postures closest to 90º elbow flexion, 90º glenohumeral flexion and 90º glenohumeral abduction, respectively, were selected for further analysis (Chaffin et al., 2006). A resting period of one minute was taken between different angle measurements while a two to five minutes break took place between different postural combinations. To avoid fatigue, the glenohumeral flexion and elbow flexion measurements were not performed sequentially but separated by the glenohumeral abduction measurements. While honoring this principle, the measurement orders were randomized between subjects. All measurements were performed on the same day and after the no-payload case to avoid influence from fatigue.

The measured pulling forces will be termed: F_{max}^{GHF} for glenohumeral flexion, F_{max}^{GHA} for glenohumeral abduction, and F_{max}^{EF} for elbow flexion. Each force represents a direct surrogate of the muscle group's net maximum moment capability, i.e. a surrogate of strength of the muscles that span the joint in question.

[Figure 2]

Figure 2. Maximum force generation capability measurement setup for the elbow flexion direction (F_{max}^{EF}).

2.2. Computational procedures

2.2.1. Skeletal modelling

The upper extremity anatomical joint angles were calculated with the AnyBody Modeling System (AMS) v.6.0.5 (AnyBody Technology A/S, Aalborg, Denmark) with an upper extremity skeletal model taken from the 'Standing Model' from the AnyBody Managed Model Repository v.1.6.3. This model comprised the lumbar spine model based on the work of De Zee et al. (2007) and the shoulder and arm models based on the work of the Delft Shoulder Group (Van der Helm et al., 1992; Veeger et al., 1997, 1991). The pelvis segment was fixed to the thorax. The scapula was constrained to slide on the surface of the rib cage. The wrist joint was fixed at neutral angles for flexion/extension and abduction/adduction. Hence, in addition to the three rotations and three translations of the trunk segments relative to the ground, 8-DOFs were enabled in the model: the sternoclavicular articulation (3-DOFs), glenohumeral articulation (3-DOFs), the elbow flexion (1-DOF) and the forearm pronation/supination (1-DOF).

A static trial capturing each participant's anatomical reference position (as mentioned section 2.2.1) was used to geometrically scale the model based on the method by Andersen *et al*. (2010). All marker positions and segment lengths (longitudinal axis) were optimized, also including hand breadth for the hand segment. Neither pelvis width nor head height parameters were optimized. Subsequently, the method by Andersen et al. (2009) was used to reconstruct the movements of the skeletal model from the motion capture data for the dynamic trials.

2.2.2. Reachable 3-D workspace volume using alpha-shapes

The reachable 3-D point cloud for each of the four load cases, each combining its five tasks, was recorded as palm locations relative to the thorax anatomical reference frame. This thorax anatomical reference frame was defined along the longitudinal axis of the ellipsoid used to model the whole thoracic cage (Van der Helm et al., 1992), which is obtained from the reflective

markers on the thorax. The envelope shape was derived from the point cloud with an alpha-shape (α-shape) algorithm capable of handling non-convex point sets (Edelsbrunner and Mücke, 1994). It can be perceived as the non-convex counter part of the set's convex hull. Compared with the convex hull, the α-shape provides a better approximation of the real silhouette of the point set because it is not constrained to convexity. The alpha-complex derives from a Delaunay triangulation of a point cloud with a carving sphere of α-radius. The α-shape is the resultant non-convex boundary shape. For example, when $\alpha = \infty$, the α-shape corresponds to the convex hull, while $\alpha = 0$, it is the singular point cloud. As the α-radius decreases, the edges of the tessellation, which can no longer be circumscribed by the sphere, are removed from the tessellation.

To solve the current RWS problem, the α-radius was set according to the smallest radius of the ellipsoid used to wrap the serratus anterior muscle around the rib cage as illustrated in Figure 3. This ellipsoid is a logical choice because it represents the volume of the thorax segment (torso) in the model. Thus, its dimensions applied to the α-shape allows for carving the negative shape of the torso out of the reachable 3-D point cloud. The inherent sensitivity of the resulting α-shape to α-radius was not addressed in previously published assessments of RWSs. Given the subject-specific nature of this parameter, the α-shape volume was checked by reducing and enlarging 10% of the measured α-radius. Custom scripts for data analysis and processing were implemented in MATLAB® v.2016b (MathWorks, Natick, MA, USA), and MATLAB's *volume* function calculated the volume of each α-shape.

In cases where the RWS point cloud is fitted and approximated to a sphere centred at the glenohumeral joint (Kurillo et al., 2012; Sengupta and Das, 1998), a surface area rather than a volume is reported. Kurillo et al. (2012) suggested normalizing that envelope area by half of the surface area of a sphere with radius equal to the length of the full elbow extended upper extremity. Likewise, in this study, the volume output was normalized (V_{norm}) to the volume of a complete sphere with a radius defined as the distance between the glenohumeral joint centre and the palm of the hand.

[Figure 3]

Figure 3. Reconstruction of the reachable workspace. The α-radius is equal to the smaller radius of the ellipse obtained from the cross-section of the torso ellipsoid (left). The resultant point cloud obtained from merging five tasks trials of a specific payload case (center), along with the α-sphere, enables estimating the non-convex α-shape envelope of the RWS (right).

2.3. Statistical modelling

All statistical analyses were conducted in R (RStudio, Boston, MA, USA). Initially, the variation of the non-normalized RWS volume between each payload group was analysed. Given the reduced sample size, a Friedman test was used to test for different group medians. A post-hoc Wilcoxon signed rank test was subsequently performed pairwise to the load case groups.

For investigating dependency of the normalized RWS volume, V_{norm}, on subject-specific parameters and payload, the no-payload case data was removed and a total of five explanatory variables were considered for this study: payload (P), body-mass index (I_{BM}), maximum forces produced for glenohumeral flexion (F_{max}^{GHF}), glenohumeral abduction (F_{max}^{GHA}) and elbow flexion (F_{max}^{EF}). The rationale was to select, besides the more intuitive payload, a body-mass index variable directly related to an isolated individual anthropometric measure and three forces as surrogates of individual muscular strength. To reduce the dimensionality of the problem, the inherent anthropometric values of the upper extremity segments lengths were used to normalize the volume, thus allowing for inter-subject volume comparison.

The pairwise correlation between the response V_{norm} and the explanatory variables was investigated. To ensure the independence of these predictors and avoid multicollinearity, the payload values were normalized (P_{norm}) by dividing them by each test-subject's payload value corresponding to the second load-case. This 90° shoulder abduction measure matches the largest moment arm about the joint and seemed to be a reasonable normalizing value given that the maximum payload tolerance for each participant was not known. Meanwhile, simpler interaction models of the response V_{norm} depending on normalized payload P_{norm} and body-mass index I_{BM} or each of the maximum forces produced F_{max}^{GHF}, F_{max}^{GHA}, F_{max}^{FE} were plotted as levels of a factor against each other in order to visually appreciate possible interactions. If crossing profiles were present, they reflect interaction between the two explanatory variables plotted.

In order to assess whether the predictors interacted, second order interaction terms were included in a multiple linear regression model according to Equation (1), where the off-diagonal elements of the symmetric matrix $\mathbf{A}$, the elements of vector $\mathbf{a}$ and variable b are coefficients of the regression. Only linear terms for the predictors were included.

$$\hat{y}_i = \mathbf{X}_i^T \mathbf{A} \mathbf{X}_i + \mathbf{a}^T \mathbf{X}_i + b \tag{1}$$

where

$$\mathbf{X}_i = \begin{bmatrix} P_{norm_i} & I_{BM_i} & F_{max\,i}^{GHF} & F_{max\,i}^{GHA} & F_{max_i}^{FE} \end{bmatrix}^T$$

$$\mathbf{A} = \begin{bmatrix} 0 & \frac{A_1}{2} & \frac{A_2}{2} & \frac{A_3}{2} & \frac{A_4}{2} \\ & 0 & \frac{A_5}{2} & \frac{A_6}{2} & \frac{A_7}{2} \\ & & 0 & \frac{A_8}{2} & \frac{A_9}{2} \\ & sym & & 0 & \frac{A_{10}}{2} \\ & & & & 0 \end{bmatrix}$$

$$\mathbf{a} = \begin{bmatrix} a_1 & a_2 & a_3 & a_4 & a_5 \end{bmatrix}^T$$

By performing a single-term deletions test, or backward elimination method (Montgomery and Runger, 2003), by means of the *drop1*() function in R, enabled testing whether each interaction's effect was necessary in the model while keeping all the remaining terms. This is the equivalent of performing successive ANOVA type-II analyses. The presence of interaction effects in the model were considered significant for $p<0.05$.

Posteriorly, a Leave-One-Out Cross Validation (LOOCV) analysis was performed for each of the models by consecutively isolating one test subject. The root-mean-square error (RSME) for each of the three load cases per subject is presented as a cumulative sum of RSME for all subjects while testing for each of the mentioned linear models.

3. RESULTS

3.1. Kinematic assessment of the reachable 3-D workspace

An example of a reconstructed RWS for a no-payload case is shown in Figure 4 for different views. The RWS envelope surrounds the torso ellipsoid in a non-convex manner without penetrating it and spans the entire head region as expected for a healthy individual.

[Figure 4]

Figure 4. Reconstructed volume for the no-payload condition for one subject. The six different views: (A) Anterior; (P) Posterior; (L) Lateral; (M) Medial; (S) Superior; (I) Inferior.

The volume of each α-shape was calculated for each RWS envelope and the obtained values are presented in the histogram of Figure 5. An extension of these results are depicted in Figure 6 for all individuals. Given the division of the hand-payload conditions into four different cases, a global trend of decreasing volume as the hand payload increases is observed. An exception is subject number 6, for whom the volume slightly increased from the third to the fourth payload case. Generally, analysing this volume variation as function of payload, the performed Friedman test (χ^2=28.92,df=3) was found to be significant (p<0.001) across groups. Likewise, the pairwise comparisons performed using the Wilcoxon signed-rank test with Bonferroni adjustment were also all significant (0.012≤p≤0.023). This can indicate the hand-payload as an important, if not the main, predictor of the RWS volume.

The obtained α-radius across the ten subjects had a mean value of 0.133±0.007 m. The volume estimation decreased with decreasing α-radius and vice-versa. When compared to the volume measured with the previously defined α-radius, the relative volume variation was (mean±sd): 2.769±0.897 %, 5.305±2.427 %, 6.903±2.471 % and 5.761±1.760 % for the no-payload, first payload, second payload and third payload cases, respectively. Hence, for larger volumes as in the no-payload case (Figure 5), the sensitivity of the volume towards α-radius was the smallest.

[Figure 5]
Figure 5. The volume variation per hand-payload case for each test subject. The payload value (in kg) is indicated in the bottom of each bar. From the assessed "no load" condition plus three increasing load cases follows an overall volume reduction. The whiskers on top of each bar represent the sensitivity of the volume on the alpha parameter. In terms of relative volume variation (percentage), the no-load case is the case with the least sensitivity.

[Figure 6]
Figure 6. Three (frontal, lateral and top) views for all ten test-subjects for the three payload cases.

3.2. Dynamometric assessment of the maximum force generation capability

The collected data on maximum force generation capability were the following (mean±sd): F_{max}^{GHF}=265.4±64.5 N; F_{max}^{GHA}=274.2±37.9 N; F_{max}^{EF}=455.3±163.6 N. The respective angles for each force measurement were (mean±sd): 71.2º±10.7º glenohumeral flexion; 61.7º±15.5º glenohumeral abduction; 97.3º±9.9º elbow flexion. Regarding the normalized external force vector as measured by the reflective markers placed on the force sensor, the ratio between vertical and horizontal force components was found to be (mean±sd): 13.5±11.2 for glenohumeral flexion; 22.0±12.0 for glenohumeral abduction; 8.4±3.0 for elbow flexion. These data support that the force vectors were mainly vertical.

The scatter plot matrix for the normalized volume data with the no-payload case removed is visualized in Figure 7. Regarding the pairwise relationship between the response V_{norm} and the potential explanatory variables, V_{norm} was found to be strongly inversely correlated to P (r=−0.736,p<0.001), weakly inversely correlated to I_{BM} (r=−0.279,p=0.136), to F_{max}^{GHF} (r=−0.110,p=0.562) and to F_{max}^{EF} (r=−0.198,p=0.295), and not correlated to F_{max}^{GHA} (r=−0.048,p=0.801).

Since P was moderately correlated with both I_{BM} (r=0.607,p<0.001) and F_{max}^{EF} (r=0.651,p<0.001), and weakly correlated to both F_{max}^{GHF} (r=0.361,p=0.050) and F_{max}^{GHA} (r=0.199,p=0.291), it might suggest collinearity in the data, i.e. essentially variable dependency

between P, I_{BM} and F_{max}^{EF}; on the other hand, P_{norm} being strongly inversely correlated to V_{norm} (r=-0.807,p<0.001), it did not correlate with any of the other predictors: I_{BM} (r=-0.048,p=0.802), F_{max}^{GHF} (r=-0.008,p=0.966), F_{max}^{GHA} (r=-0.089,p=0.639) and F_{max}^{EF} (r=-0.015,p=0.937). The remaining I_{BM} presented moderate correlation with F_{max}^{EF} (r=0.542,p=0.002) but weak correlation with F_{max}^{GHF} (r=0.318,p=0.087) and no correlation with F_{max}^{GHA} (r=0.085,p=0.657); F_{max}^{GHA} was weakly correlated to both F_{max}^{GHF} (r=0.403,p=0.027) and F_{max}^{EF} (r=0.476,p=0.008); and F_{max}^{GHF} was moderately correlated to F_{max}^{EF} (r=0.661,p<0.001).

[Figure 7]

Figure 7. Pairwise correlations for the response (normalized volume V_{norm}) and respective explanatory variables to include in the desired linear model with the no-payload case data removed. In the upper right triangle of the matrix it is possible to observe the scattered data with pairwise fitting linear models. Respectively, in the lower left triangle of the matrix one can observe the correlation coefficient r and the p-value associated with a ANOVA test applied on each linear model.

3.3. Multiple linear regression model

It is graphically shown in Figure 8 and Figure 9 how some of the selected explanatory variables, namely payload P_{norm} could potentially interact with I_{BM} and with $F_{max}^{GHF}/F_{max}^{GHA}/F_{max}^{EF}$, respectively. Since these predictors could interact even though they did not correlate, the crossing linear profiles suggested the presence of interactions between them.

[Figure 8]

Figure 8. Plots for the appreciation of potential interaction effects between payload P_{norm} and body-mass-index I_{BM}, might interact upon the estimation of the normalized volume V_{norm}. (Left column) The V_{norm} plotted against P_{norm} using I_{BM} as a factor; (Right column) The V_{norm} plotted against I_{BM} using P_{norm} as a factor. The crossing profiles potentially indicate interaction between variables.

[Figure 9]

Figure 9. Plots for the appreciation of potential interaction effects between payload P_{norm} and maximum forces produced F_{max}^{GHF}, F_{max}^{GHA} and F_{max}^{EF}, might interact upon the estimation of the normalized volume V_{norm}. (Left column) The V_{norm} plotted against P_{norm} using each F_{max}^{GHF}, F_{max}^{GHA} and F_{max}^{EF} as a factor, separately; (Right column) The V_{norm} plotted against each F_{max}^{GHF}, F_{max}^{GHA} and F_{max}^{EF} using P_{norm} as a factor. The crossing profiles potentially indicate interaction between variables.

Subsequently, the backward elimination method performed to assess the significance of all interaction and additive terms was used for statistical modelling. The deleted single-terms are shown in Figure 10 in decreasing order of significance along with the LOOVC analysis results. With the exception of the P_{norm} and I_{BM} terms alone, it was found that the presence of all interaction effects and remaining isolated predictor terms in the model were not significant (p>0.05). Hence, the additive model composed of P_{norm} (F=73.740,p<0.001) and I_{BM} (F=11.008,p=0.003) predictors was significant (F(2,27)=41.11, p<0.001,R_{adj}^2=0.7345). Moreover, it was the model with the lowest cumulative root-mean-square error (RMSE) among all models in the LOOVC analysis.

[Figure 10]

Figure 10. LOOVC analyses on the different interaction models by increasing order of term statistical significance. The label below each bar corresponds to the dropped term in the respective model. The terms composing a given model are all the labels of the bars at the right side of the given model's bar, and the R_{adj}^2 value for that particular

model is shown in the top of its bar. The best model, with lowest cumulative root-mean-squared error (RMSE) is represented by (*).

The regression model, function of both P_{norm} and I_{BM}, is presented in Equation (2).

$$V_{norm} = 0.58988 - 0.26024P_{norm} - 0.00719I_{BM} \quad (2)$$

The analysis of the model's residual values against fitted values and theoretical data quantiles can be observed in Figure 11. The points scatter randomly around both horizontal and identity line for the model of Equation (2), not showing signs of clustering among load case groups.

[Figure 11]

Figure 11. Residual-fitted values and Q-Q plots for the additive regression model with P_{norm} and I_{BM} as predictors. Each colour of the data points correspond to a different payload case. The model showed a better scattered data points and no clustering in both plots, thus supporting evidence for a good model.

The performance of the model V_{norm} as a function of the two significant predictors P_{norm} and I_{BM}, is illustrated in Figure *12*.

[Figure *12*]

Figure 12. The normalized volume predictions (black triangles) obtained from the additive model P_{norm} and I_{BM} for all hand-payload cases (excluding the no-payload) for each test-subject. The payload value (in kg) is indicated in the bottom of each bar. The whiskers on top of each bar represent the sensitivity of the volume on the alpha parameter.

4. DISCUSSION

In this study, a new movement protocol for the assessment of the RWS was designed. It enabled capturing the close-to-torso reachable region which subsequently helped retrieving the non-convex shape of the RWS envelope. The results indicate that the hand-payload has a major influence on the obtained RWS volume across nearly all subjects as evidenced by the significance of the tests presented in section 3.1: the volume decreases with increasing payload. However, this trend was absent in one test-subject for two payload cases, which might be related to the payload increment chosen upon the initial one-repetition abduction test or a variation in the effort by the subject.

The non-normalized volume values obtained in the no-payload case (Figure 5) are slightly below the values previously reported for full no-payload RWS (Klopčar et al., 2007; Klopčar and Lenarčič, 2005), but closer to the volume value reported by Matthew et al. (2015) for a healthy individual. All these authors indirectly estimated the no-payload RWS volume from kinematic biomechanical models, based on extreme trajectories drawn in the three anatomical planes along with subject-specific data of active anatomical ROM. The slight volume discrepancy might come from the difficulty of guaranteeing that the movement protocol proposed in this work entirely spans the real RWS. In the light of the results for the no-payload RWS, it was found that the ratio between that actual volume and the total spherical volume – with radius equal to the upper extremity length – is approximately one third, instead of one half. This not only depends on each subject-specific active ROM, but is also influenced by the α-radius and by the density of the RWS workspace point cloud.

Moreover, the half-spherical shape of the RWS shrinks with increasing payload since higher payloads generate larger moments about the shoulder joint Figure 6). An hourglass shaped RWS transformation was expected. However, the over-head and over-shoulder regions were

also affected. That may derive from the fact that all tasks start from the anatomical reference position, so these regions could only be spanned during the close-to-torso and free-motion tasks. The lateral aspects of the RWS shape, those related to abduction types of motion, tend to decrease more than the frontal one.

The pairwise correlations between the assessment variables (section 3.2) showed that V_{norm} was strongly correlated to P as the best predictor of RWS volume. The remaining predictors I_{BM}, F_{max}^{GHF}, F_{max}^{GHA} and F_{max}^{EF} were poorly or not correlated with V_{norm}. It was also found that P was moderately correlated to both I_{BM} and F_{max}^{EF}. Nonetheless, normalizing P by the 90º abduction payload as a reference to a maximum individual payload tolerance proved to be effective to remove potential multicollinearity, while maintaining a strong inverse correlation with V_{norm}. It should be noted that this 90º abduction payload does not represent the real maximum payload tolerance, which is difficult to define and measure, but it allows comparison between subjects. Besides P_{norm}, the lack of association between V_{norm} and the remaining explanatory variables did not imply that interactions were absent when trying to estimate the volume. That was effectively demonstrated later in section 3.3, by the crossing profiles presented in Figure 8 and Figure 9. Weak and moderate correlation was also found between I_{BM} and F_{max}^{GHF} and F_{max}^{EF} even though previous findings by D'Souza et al. (2012) suggested that predicting strength from anthropometric data was nearly impossible.

The statistical modelling of the RWS volume by the backward elimination method along with the LOOCV analysis (Figure 10) confirmed P_{norm} as the most relevant volume predictor. This parameter alone was able to explain approximately half of the variation in the volume data, supporting the effect of payload on the RWS as advocated by Park (2007) and Johnston et al. (2015). Additionally, statistical significance was clear with respect to the addition of an anthropometric measure for a more accurate estimation of the volume: the second predictor I_{BM} improved the model's response by explaining 10% more variation in the data (Fig. 10). Such finding is supported by the study of Park (2007). The dependency of the RWS on subject-specific strength was, however, not statistically significant in contrast with previous findings for both healthy (Park, 2007) and non-healthy individuals (Han et al., 2015). Still, bearing in mind that payload was normalized by the 90º abduction payload as a reference of maximum individual payload tolerance, it may relate to subject-specific strength. Yet, a large data set might be required to prove so. The back elimination method is also type II error-prone – due to the two-way ANOVA – it is possible that some interaction effects might not have been detectable in the data as suggested by Figure 8 and Figure 9. In the interest of simple regression models, it is an advantage that an extra set of subject-specific strength-related measurements is not necessary, besides payload and body-mass-index. Another option to further investigate the relations between these parameters could be through principal component analysis on a larger data set.

The study design has some limitations. When acquiring data, it was not possible to maintain a perfectly vertical trunk posture, and back tilting compensation movements were present for heavier loads. This was addressed by using the thorax rather than the pelvis as the RWS origin. However, it is unclear whether the maximal muscle forces exerted during these compensation movements correlate with the forces of the strength measurements in which the back was supported. In addition, it must be emphasized that the reliability of the RWS measurements was not investigated for each specific load case. The same way, whether the starting posture of the arm during task performance (e.g. from top/overhead to down/waist and from lateral to medial) affects fatigue and consequently the RWS volume metrics still remains unanswered. This would require a longer assessment period and prolong the study where measurement of the four load cases already involves four distinct measurement days. The scheduling of the maximal effort tests is inevitably a compromise between recovery time to avoid fatigue and the consideration of possible differences in conditions between multiple days. Therefore, apart from the

randomization of task trials for every individual and load case, fatigue might have masked parts of the real volume. Another limitation that must not be ignored, arises from the use of the dumbbells since, as the weight increases, so does the dumbbell volume and consequently marginally decreases the RWS volume at the close-to-torso region specially during the shower task. The use of wrist-adjustable weight straps could help minimizing such error. Last but not least, readers should be careful while extrapolating this regression model to the usual lightweight payloads associated with common ADL.

5. CONCLUSIONS

In conclusion, this study presented a new experimental protocol which enabled capturing the close-to-torso region in addition to the far-from-torso region. A method for choosing α-radius retrieving the non-convex shape exploited by the experimental protocol was also proposed. Altogether, the experiment supported that maximum RWS volume is not a kinematic measure only based on anthropometrics but rather a more complex and kinetic function also dependent on hand payload.

Protocols of this type can potentially improve digital manikins and thereby work environment and exoskeletons design, in addiction to quantifying the impairment following certain upper extremity disorders. The minimized setup costs for assessing the RWS may, along with new motion capture technologies such as the Kinect™ (Microsoft, Redmond, Washington, US), enable low-budget experiments as demonstrated by some authors (Han et al., 2013; Kurillo et al., 2013a, 2013b).

6. ACKNOWLEDGEMENTS

This work was supported by Patient@Home (www.patientathome.dk), a strategic platform for research and innovation, supported by the Danish Agency for Science, Technology and Innovation.

REFERENCES

Andersen, M.S., Damsgaard, M., MacWilliams, B., Rasmussen, J., 2010. A computationally efficient optimisation-based method for parameter identification of kinematically determinate and over-determinate biomechanical systems. Comput. Methods Biomech. Biomed. Engin. 13, 171–183. doi:10.1080/10255840903067080

Andersen, M.S., Damsgaard, M., Rasmussen, J., 2009. Kinematic analysis of over-determinate biomechanical systems. Comput. Methods Biomech. Biomed. Engin. 12, 371–384. doi:10.1080/10255840802459412

Chaffin, D.B., Andersson, G.B.J., Martin, B.J., 2006. Occupational Biomechanics, 4th ed. ed. Wiley, New Jersey, USA.

D'Souza, S., Rasmussen, J., Schwirtz, A., 2012. Multiple linear regression to develop strength scaled equations for knee and elbow joints based on age, gender and segment mass. Int. J. Hum. Factors Model. Simul. 3, 32–47. doi:10.1504/IJHFMS.2012.050071

de Zee, M., Hansen, L., Wong, C., Rasmussen, J., Simonsen, E.B., 2007. A generic detailed rigid-body lumbar spine model. J. Biomech. 40, 1219–1227. doi:10.1016/j.jbiomech.2006.05.030

Edelsbrunner, H., Mücke, E., 1994. Three-dimensional alpha shapes. ACM Trans. Graph. 13, 43–72. doi:10.1145/174462.156635

Han, J.J., de Bie, E., Nicorici, A., Abresch, R.T., Bajcsy, R., Kurillo, G., 2015. Reachable workspace reflects dynamometer-measured upper extremity strength in FSHD. Muscle

Nerve 2, 1–8. doi:10.1002/mus.24651
Han, J.J., Kurillo, G., Abresch, R.T., Nicorici, A., Bajcsy, R., 2013. Validity, Reliability, and Sensitivity of a 3D Vision Sensor-based Upper Extremity Reachable Workspace Evaluation in Neuromuscular Diseases. PLoS Curr. 1–21. doi:10.1371/currents.md.f63ae7dde63caa718fa0770217c5a0e6
Johnston, H., Dewis, C., Kozey, J., 2015. Effect of hand-held loads on the maximum reach envelope. Occup. Ergon. 12, 179–187. doi:10.3233/OER-160234
Klopčar, N., Lenarčič, J., 2005. Kinematic Model for Determination of Human Arm Reachable Workspace. Meccanica 40, 203–219. doi:10.1007/s11012-005-3067-0
Klopčar, N., Tomšič, M., Lenarčič, J., 2007. A kinematic model of the shoulder complex to evaluate the arm-reachable workspace. J. Biomech. 40, 86–91. doi:10.1016/j.jbiomech.2005.11.010
Kurillo, G., Chen, A., Bajcsy, R., Han, J.J., 2013a. Evaluation of upper extremity reachable workspace using Kinect camera. Technol. Heal. Care 21, 641–656. doi:10.3233/THC-130764
Kurillo, G., Han, J.J., Abresch, R.T., Nicorici, A., Yan, P., Bajcsy, R., 2012. Development and Application of Stereo Camera-Based Upper Extremity Workspace Evaluation in Patients with Neuromuscular Diseases. PLoS One 7. doi:10.1371/journal.pone.0045341
Kurillo, G., Han, J.J., Obdržálek, Š., Yan, P., Abresch, R.T., Nicorici, A., Bajcsy, R., 2013b. Upper Extremity Reachable Workspace Evaluation with Kinect, in: Medicine Meets Virtual Reality. pp. 247–253. doi:10.3233/978-1-61499-209-7-247
Lenarcic, J., Umek, A., 1994. Simple model of human arm reachable workspace. IEEE Trans. Syst. Man. Cybern. 24, 1239–1246. doi:10.1109/21.299704
Matthew, R.P., Kurillo, G., Han, J.J., Bajcsy, R., 2015. Calculating Reachable Workspace Volume for Use in Quantitative Medicine, in: Agapito, L., Bronstein, M.M., Rother, C. (Eds.), ECCV 2014 Workshops, Part III, Lecture Notes in Computer Science. Springer International Publishing, Cham, pp. 570–583. doi:10.1007/978-3-319-16199-0_40
Montgomery, D.C., Runger, G.C., 2003. Applied Statistics and Probability for Engineers, 3rd ed. ed. John Wiley & Sons, Inc, USA.
Park, W., 2007. Biomechanically Based Workspace Generation Considering Joint Muscular Strengths, Body Weight and Hand Load Weight, in: Digital Human Modeling for Design and Engineering Conference and Exhibition. Seattle, Washington, USA. doi:10.4271/2007-01-2496
Rosen, J., Perry, J.C., Manning, N., Burns, S., Hannaford, B., 2005. The human arm kinematics and dynamics during daily activities - toward a 7 DOF upper limb powered exoskeleton, in: ICAR '05. Proceedings., 12th International Conference on Advanced Robotics, 2005. IEEE, Seattle, WA, United States, pp. 532–539. doi:10.1109/ICAR.2005.1507460
Schiele, A., van der Helm, F.C.T., 2006. Kinematic design to improve ergonomics in human machine interaction. IEEE Trans. Neural Syst. Rehabil. Eng. 14, 456–69. doi:10.1109/TNSRE.2006.881565
Sengupta, a K., Das, B., AK, S., Das, B., 2000. Maximum reach envelope for the seated and standing male and female for industrial workstation design. Ergonomics 43, 1390–1404. doi:10.1080/001401300421824
Sengupta, A., Das, B., 1998. A model of three dimensional maximum reach envelope based on structural anthropometric measurements, in: Advances in Occupational Ergonomics and Safety. IOS Press, pp. 256–259.
Sengupta, A.K., Das, B., 2004. Determination of worker physiological cost in workspace reach envelopes. Ergonomics 47, 330–342. doi:10.1080/00140130320000157850
Siciliano, B., Sciavicco, L., Villani, L., Oriolo, G., 2009. Robotics: Modelling, Planning and Control, Soft Computing. Springer-Verlag, London. doi:10.1007/978-1-84628-642-1
Van der Helm, F.C.T., Veeger, H.E.J., Pronk, G.M., Van der Woude, L.H.V., Rozendal, R.H.,

1992. Geometry parameters for musculoskeletal modelling of the shoulder system. J. Biomech. 25, 129–144. doi:10.1016/0021-9290(92)90270-B
Veeger, H.E.J., Van Der Helm, F.C.T., Van Der Woude, L.H.V., Pronk, G.M., Rozendal, R.H., 1991. Inertia and muscle contraction parameters for musculoskeletal modelling of the shoulder mechanism. J. Biomech. 24, 615–629. doi:10.1016/0021-9290(91)90294-W
Veeger, H.E.J., Yu, B., An, K.-N., Rozendal, R.H., 1997. Parameters for modeling the upper extremity. J. Biomech. 30, 647–652. doi:10.1016/S0021-9290(97)00011-0
Yang, J., Abdel-Malek, K., Nebel, K., 2005. Reach envelope of a 9-degree-of freedom model of the upper extremity. Int. J. Robot. Autom. 20, 240–260.

Figure 1

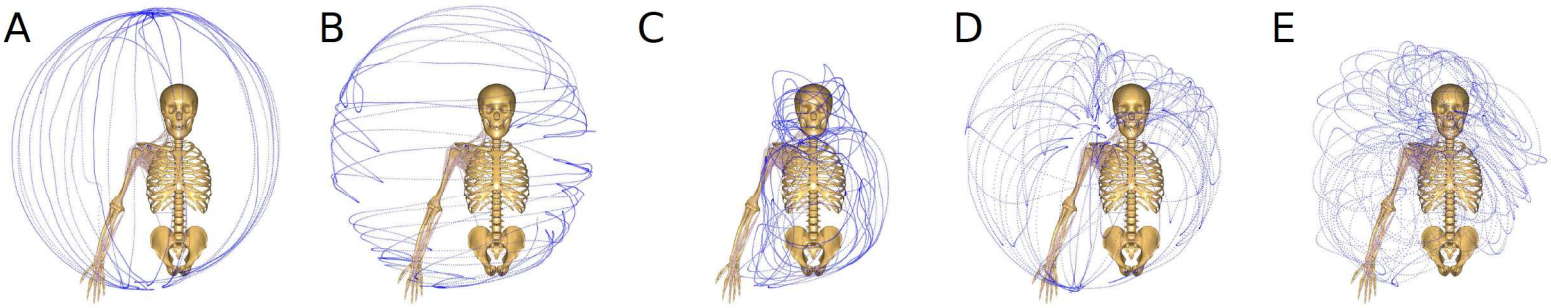

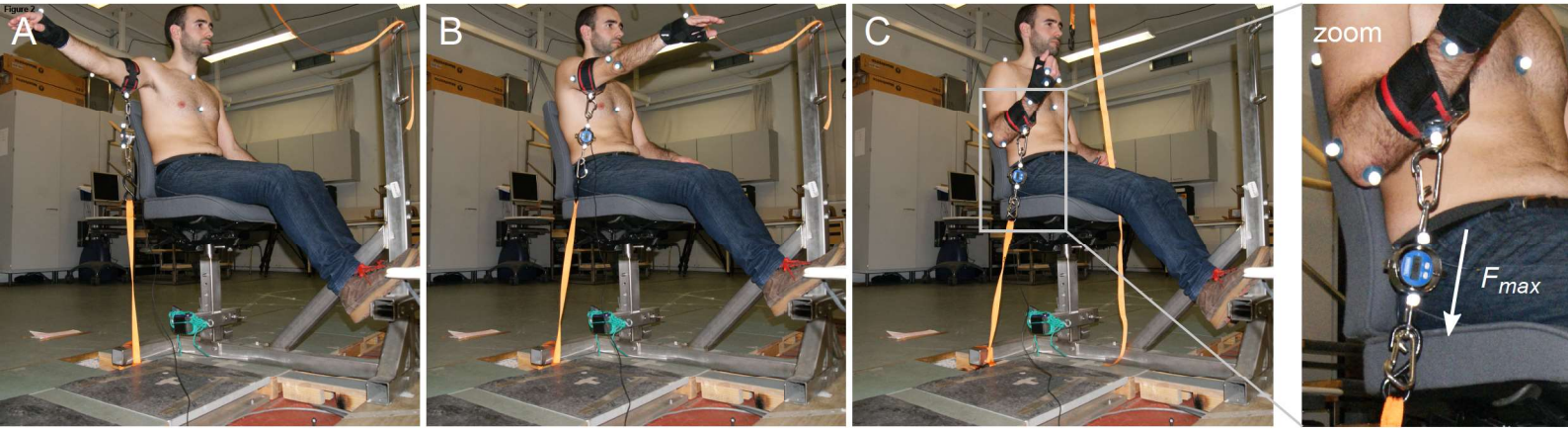
A
B
C
zoom
F_{max}

Figure 3

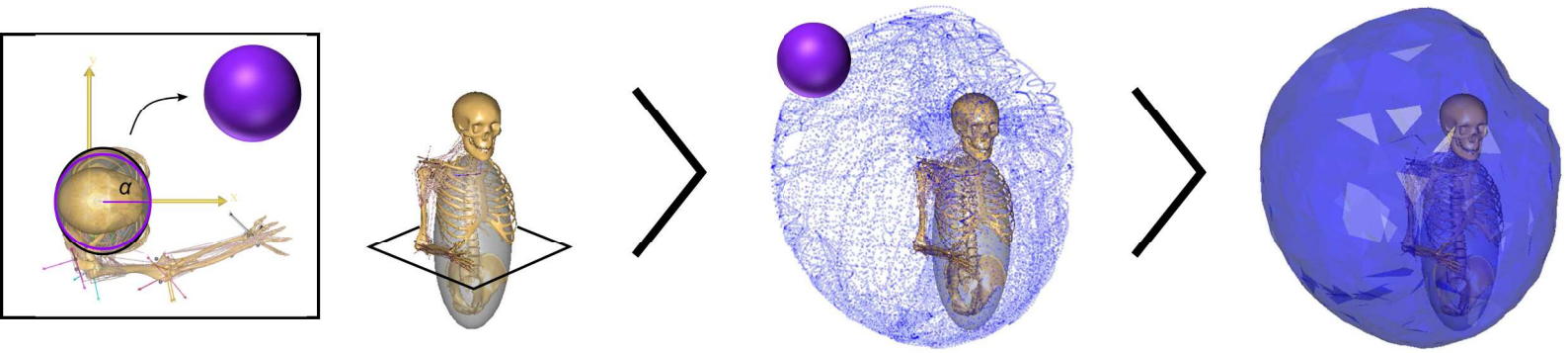

Figure 4

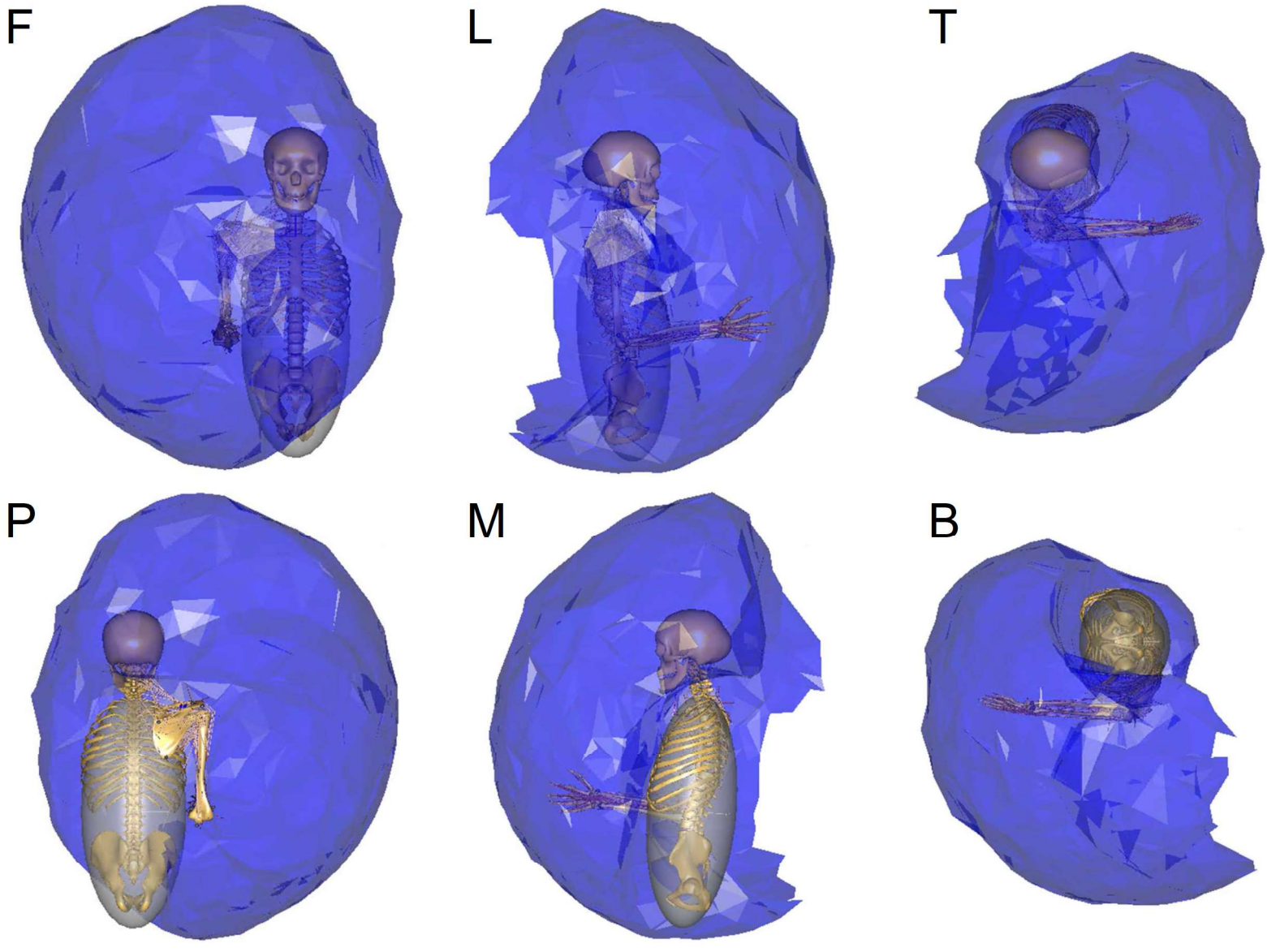

Figure 5

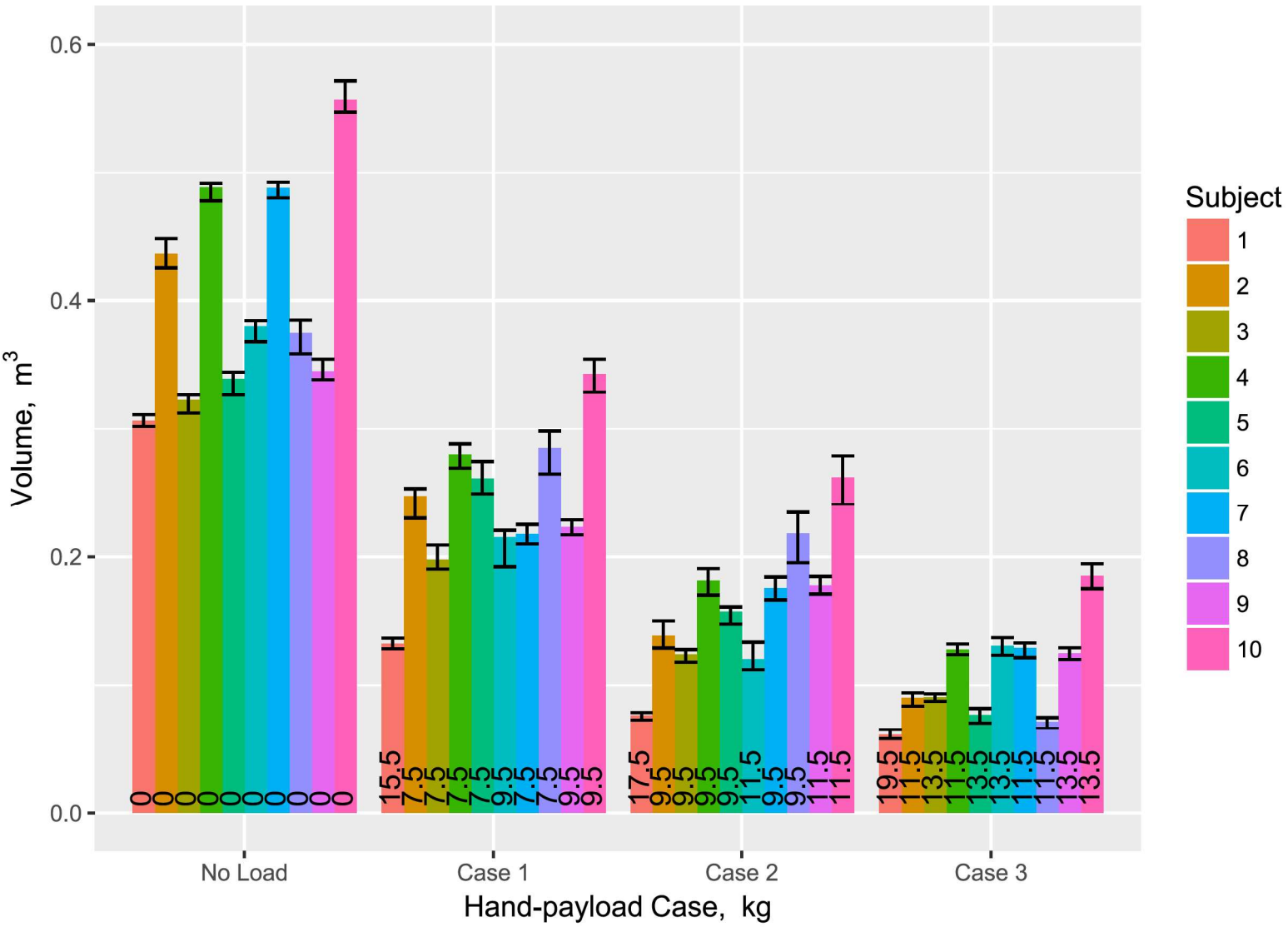
0.6
0.4
0.2
0.0
Volume, m3
0
0
0
0
0
0
0
0
0
0
15.5
7.5
7.5
7.5
7.5
9.5
7.5
7.5
9.5
9.5
17.5
9.5
9.5
9.5
9.5
11.5
9.5
9.5
11.5
11.5
19.5
11.5
13.5
11.5
13.5
13.5
11.5
11.5
13.5
13.5
No Load
Case 1
Case 2
Case 3
Hand-payload Case, kg
Subject
1
2
3
4
5
6
7
8
9
10

Figure 6

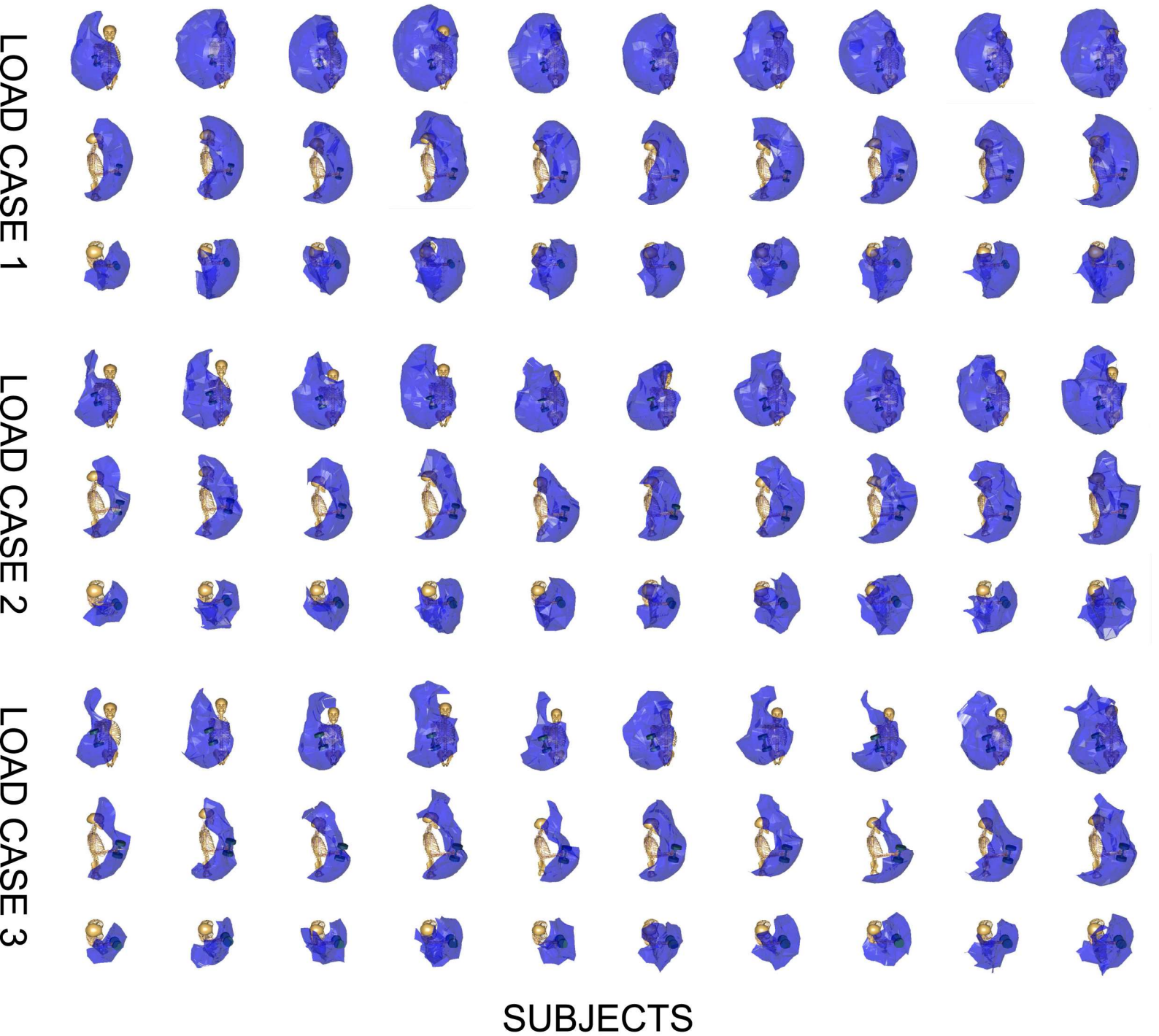

Figure 7 - R2

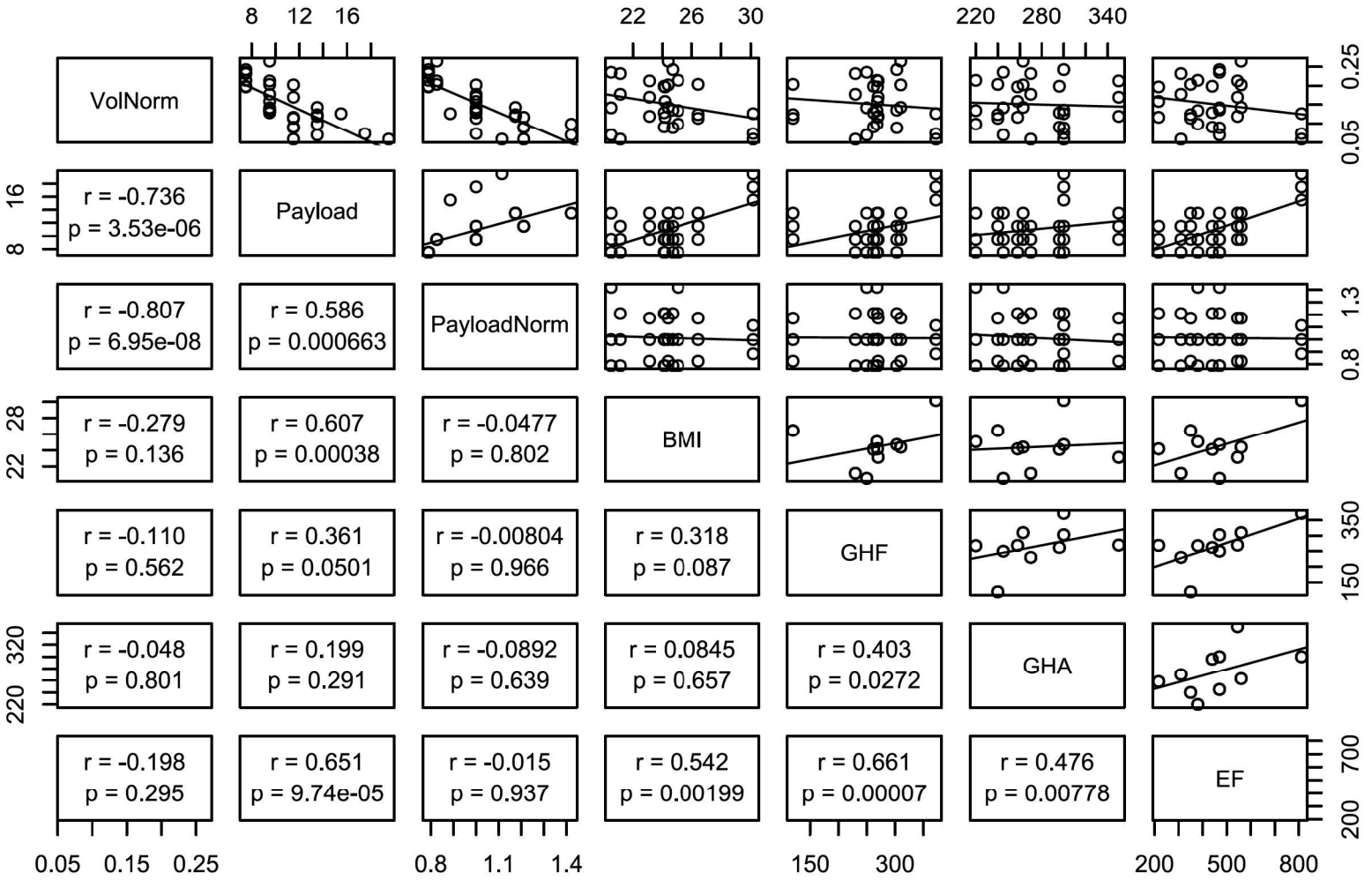
VolNorm
Payload
PayloadNorm
BMI
GHF
GHA
EF
r = -0.736
p = 3.53e-06
r = -0.807
p = 6.95e-08
r = 0.586
p = 0.000663
r = -0.279
p = 0.136
r = 0.607
p = 0.00038
r = -0.0477
p = 0.802
r = -0.110
p = 0.562
r = 0.361
p = 0.0501
r = -0.00804
p = 0.966
r = 0.318
p = 0.087
r = -0.048
p = 0.801
r = 0.199
p = 0.291
r = -0.0892
p = 0.639
r = 0.0845
p = 0.657
r = 0.403
p = 0.0272
r = -0.198
p = 0.295
r = 0.651
p = 9.74e-05
r = -0.015
p = 0.937
r = 0.542
p = 0.00199
r = 0.661
p = 0.00007
r = 0.476
p = 0.00778
8 12 16
22 26 30
220 280 340
0.05 0.25
8 16
0.8 1.3
22 28
150 350
220 320
200 700
0.05 0.15 0.25
0.8 1.1 1.4
150 300
200 500 800

Figure 8 - R2

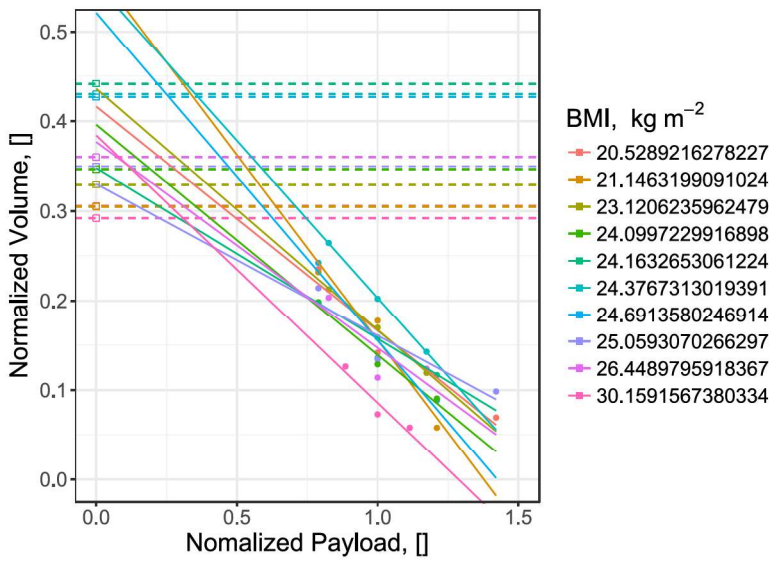
Normalized Volume, []
0.5
0.4
0.3
0.2
0.1
0.0
0.0
0.5
1.0
1.5
Nomalized Payload, []
BMI, kg m^{-2}
20.5289216278227
21.1463199091024
23.1206235962479
24.0997229916898
24.1632653061224
24.3767313019391
24.6913580246914
25.0593070266297
26.4489795918367
30.1591567380334

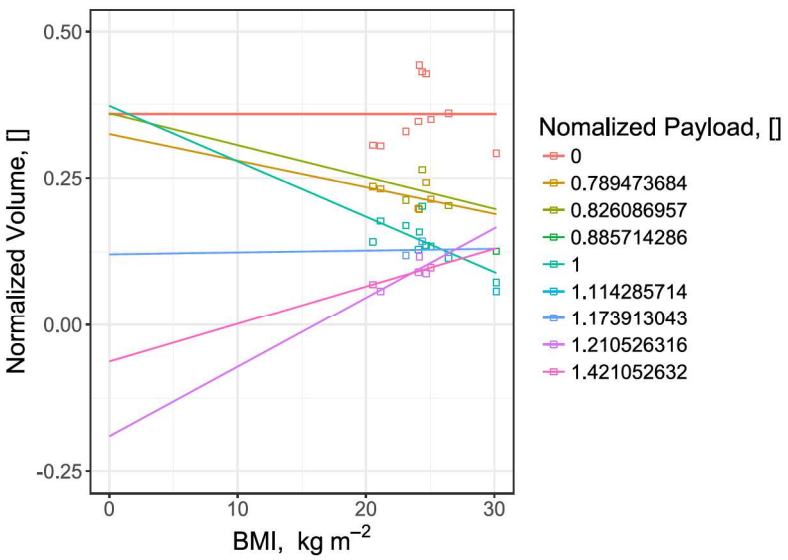
Normalized Volume, []
0.50
0.25
0.00
-0.25
0
10
20
30
BMI, kg m^{-2}
Nomalized Payload, []
0
0.789473684
0.826086957
0.885714286
1
1.114285714
1.173913043
1.210526316
1.421052632

Figure 9 - R2

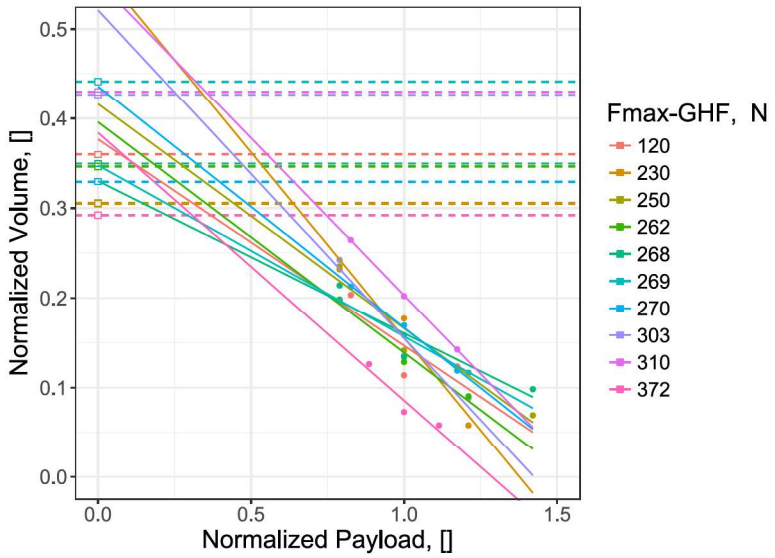
Normalized Volume, []
Normalized Payload, []
0.0
0.1
0.2
0.3
0.4
0.5
0.0
0.5
1.0
1.5

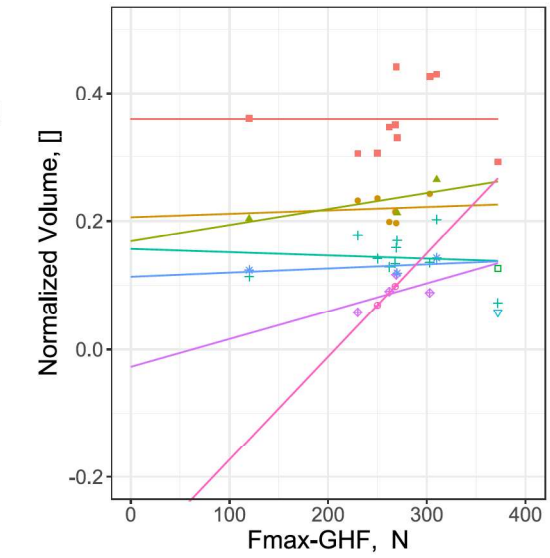
Fmax-GHF, N
120
230
250
262
268
269
270
303
310
372

Normalized Volume, []
Fmax-GHF, N
-0.2
0.0
0.2
0.4
0
100
200
300
400

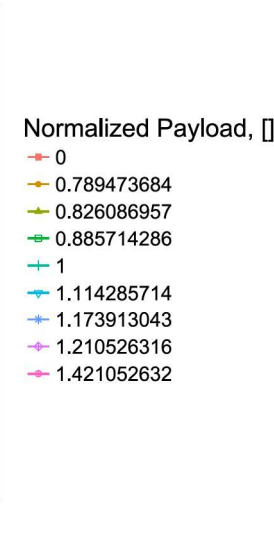
Normalized Payload, []
0
0.789473684
0.826086957
0.885714286
1
1.114285714
1.173913043
1.210526316
1.421052632

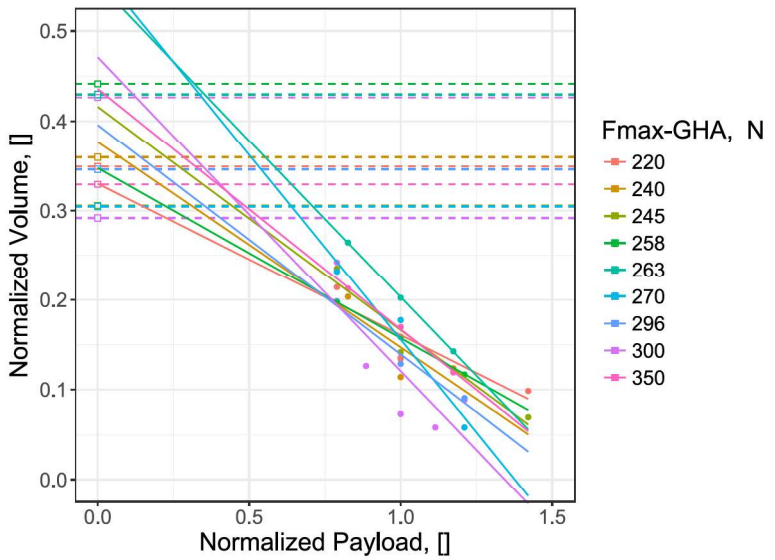
Normalized Volume, []
Normalized Payload, []
0.0
0.1
0.2
0.3
0.4
0.5
0.0
0.5
1.0
1.5

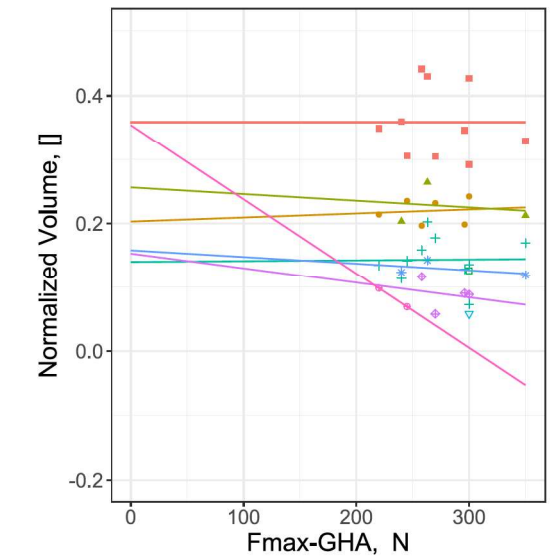
Fmax-GHA, N
220
240
245
258
263
270
296
300
350

Normalized Volume, []
Fmax-GHA, N
-0.2
0.0
0.2
0.4
0
100
200
300

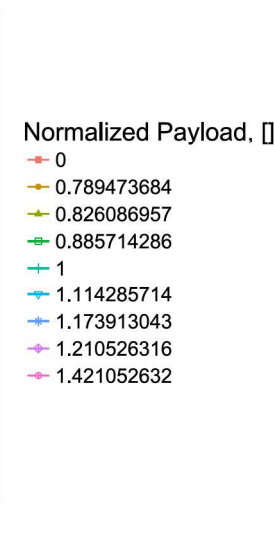
Normalized Payload, []
0
0.789473684
0.826086957
0.885714286
1
1.114285714
1.173913043
1.210526316
1.421052632

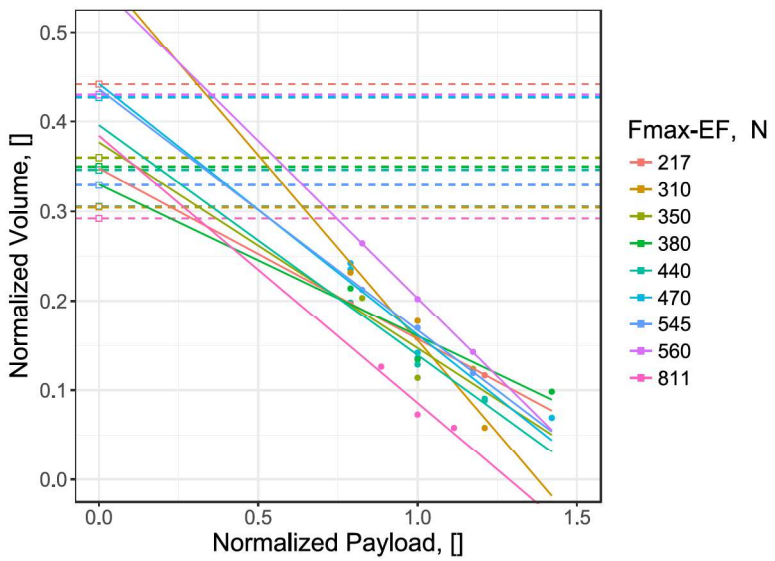
Normalized Volume, []
Normalized Payload, []
0.0
0.1
0.2
0.3
0.4
0.5
0.0
0.5
1.0
1.5

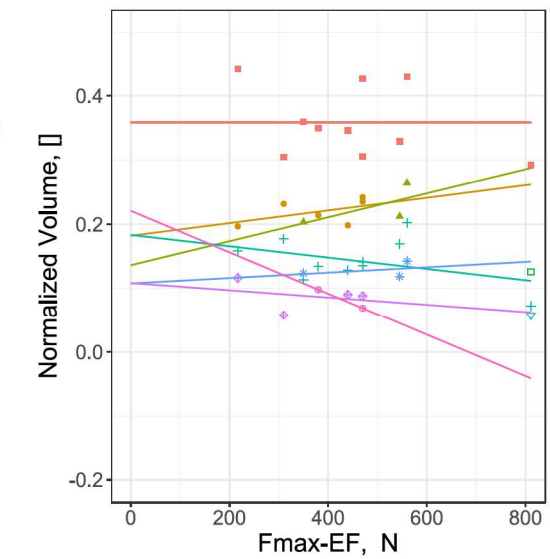
Fmax-EF, N
217
310
350
380
440
470
545
560
811

Normalized Volume, []
Fmax-EF, N
-0.2
0.0
0.2
0.4
0
200
400
600
800

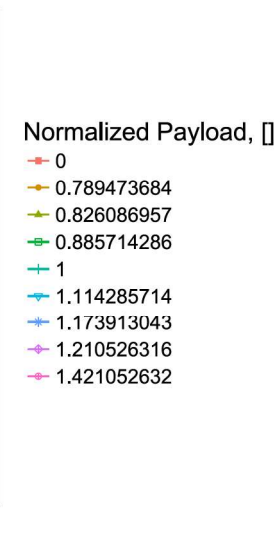
Normalized Payload, []
0
0.789473684
0.826086957
0.885714286
1
1.114285714
1.173913043
1.210526316
1.421052632

Figure 10 - R2

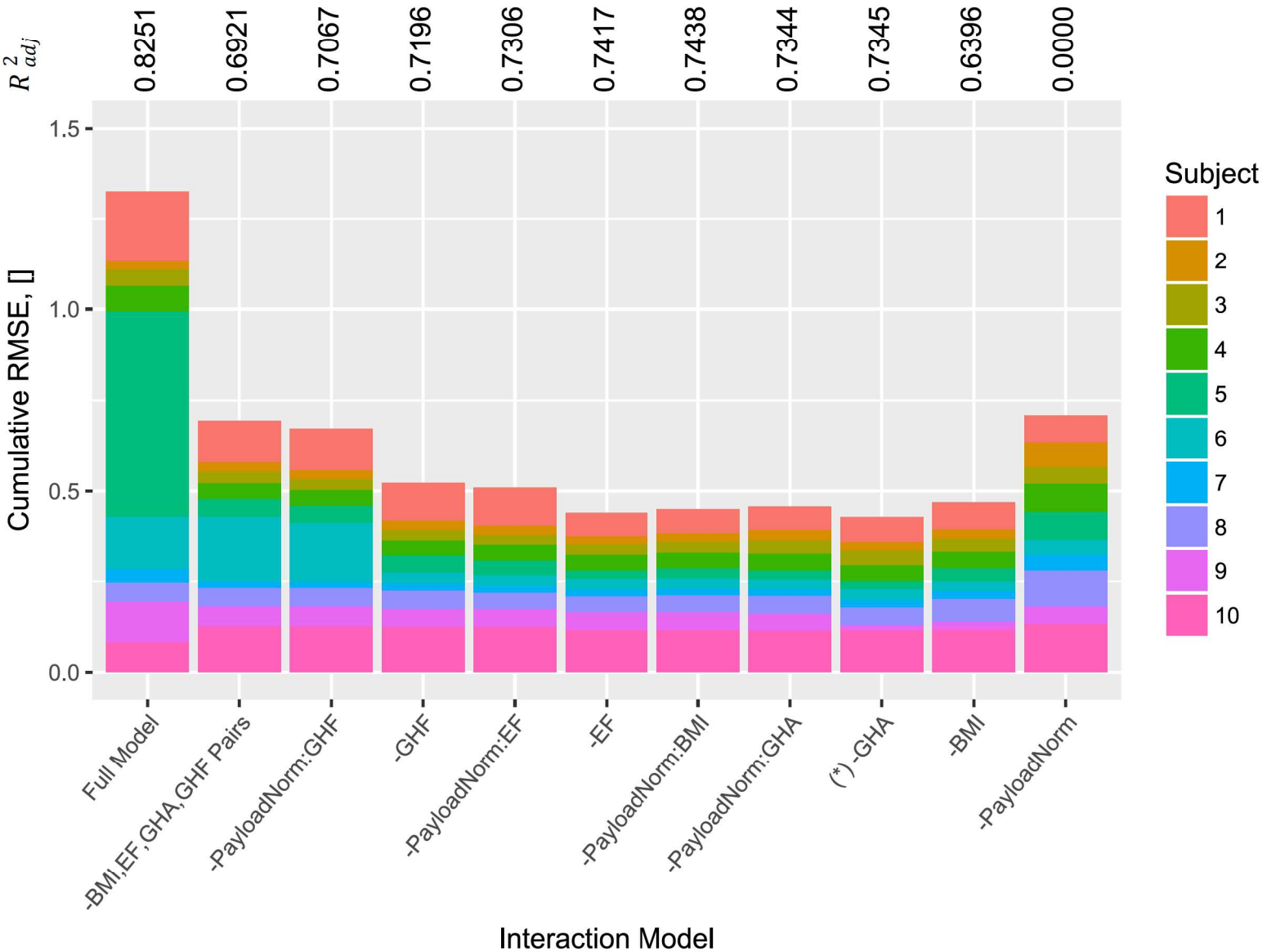
R^2_{adj}
0.8251
0.6921
0.7067
0.7196
0.7306
0.7417
0.7438
0.7344
0.7345
0.6396
0.0000
Cumulative RMSE, []
1.5
1.0
0.5
0.0
Full Model
-BMI,EF,GHA,GHF Pairs
-PayloadNorm:GHF
-GHF
-PayloadNorm:EF
-EF
-PayloadNorm:BMI
-PayloadNorm:GHA
(*) -GHA
-BMI
-PayloadNorm
Interaction Model
Subject
1
2
3
4
5
6
7
8
9
10

Figure 11 - R2

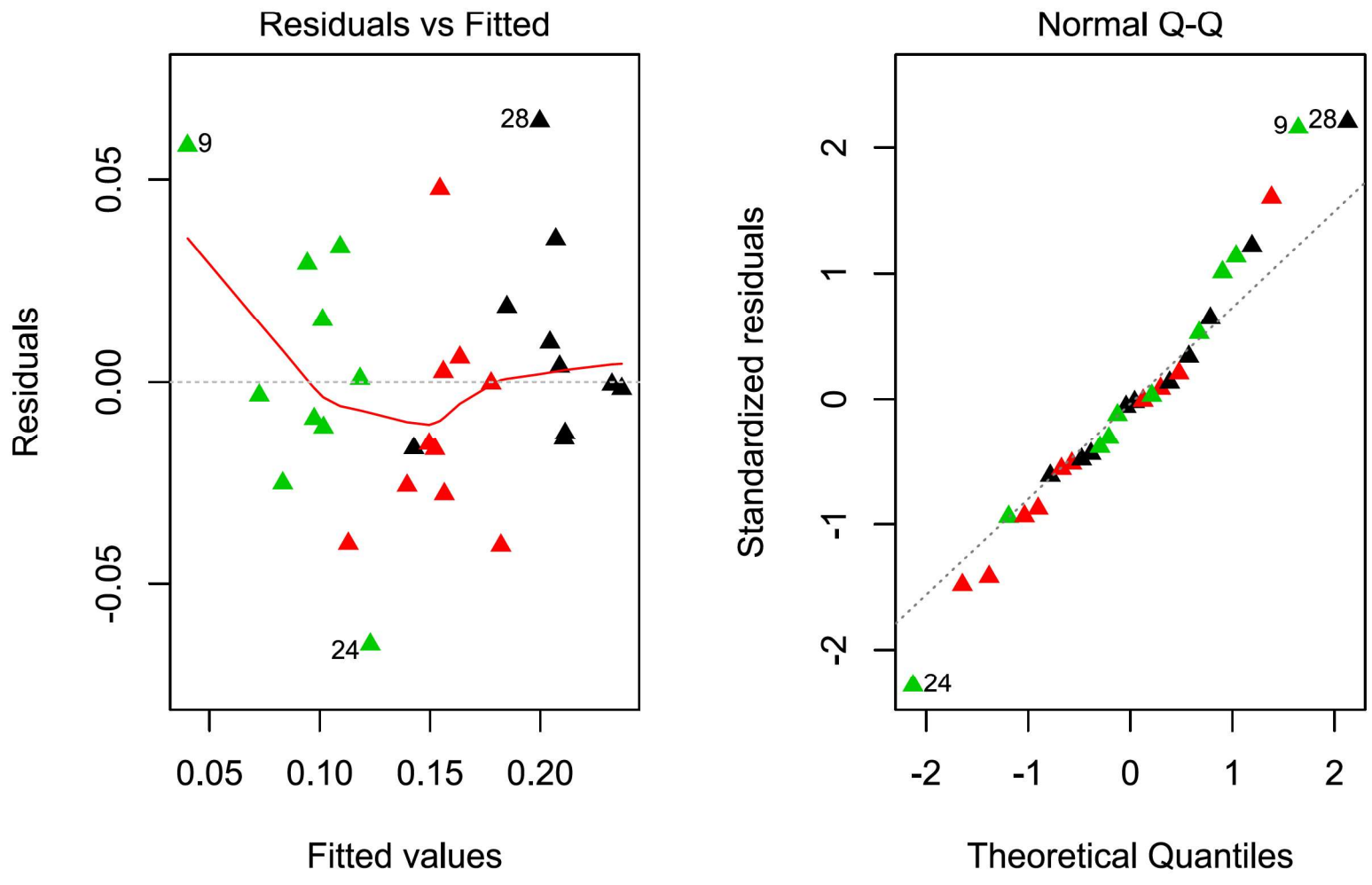
Residuals vs Fitted
Residuals
Fitted values
9
28
24
0.05
0.00
-0.05
0.05
0.10
0.15
0.20
Normal Q-Q
Standardized residuals
Theoretical Quantiles
9
28
24
2
1
0
-1
-2
-2
-1
0
1
2

Figure 12 - R2

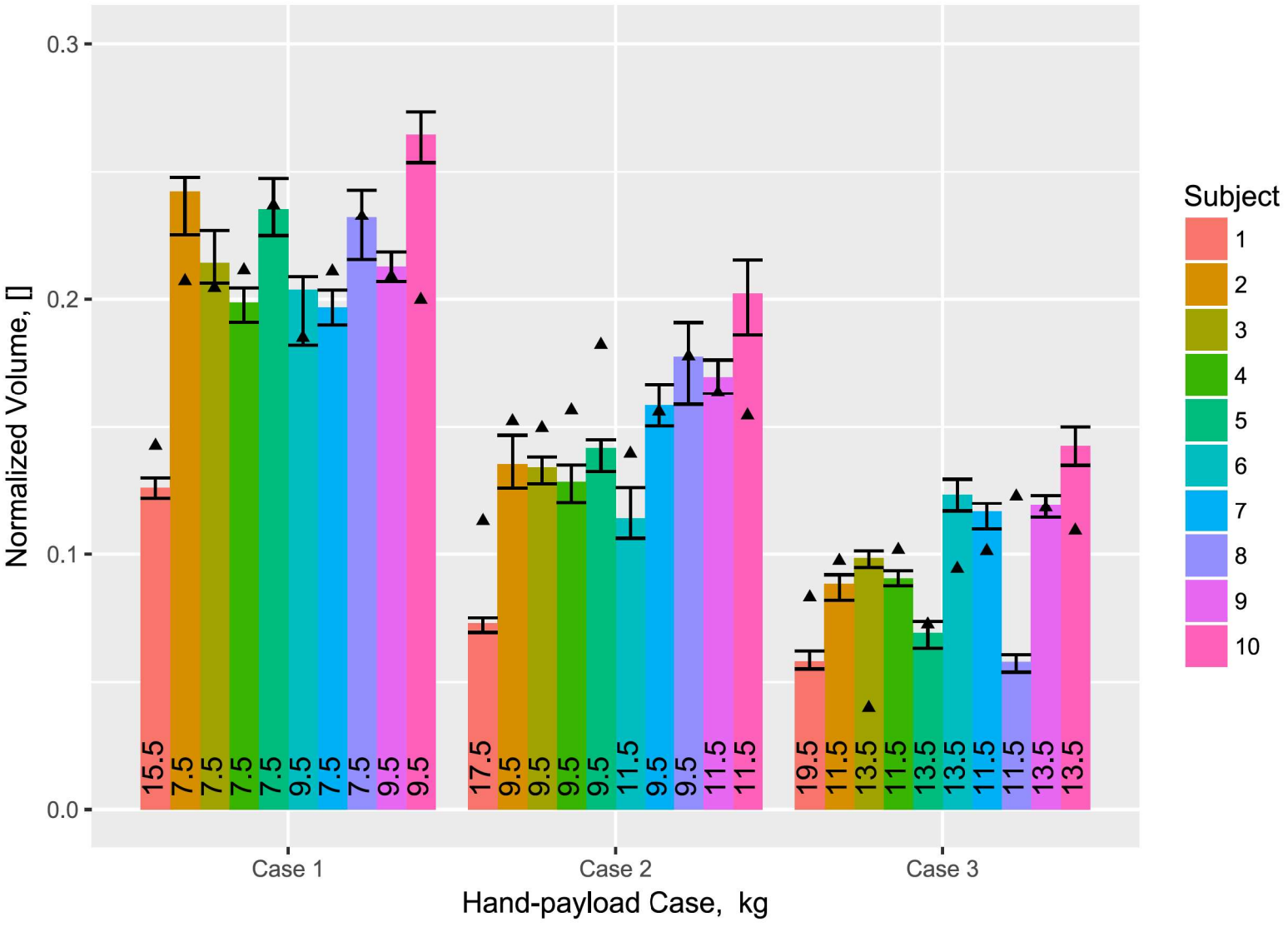
0.3
0.2
0.1
0.0
Normalized Volume, []
15.5
7.5
7.5
7.5
7.5
9.5
7.5
7.5
9.5
9.5
17.5
9.5
9.5
9.5
9.5
11.5
9.5
9.5
11.5
11.5
19.5
11.5
13.5
11.5
13.5
13.5
11.5
11.5
13.5
13.5
Case 1
Case 2
Case 3
Hand-payload Case, kg
Subject
1
2
3
4
5
6
7
8
9
10